EXPERIMENTAL INVESTIGATIONS OF A WIND TUNNEL MODEL FOR THE ANALYSIS OF FLUID-STRUCTURE INTERACTION CAUSED BY THE INFLUENCE OF LEADING-EDGE VORTEX SYSTEMS

P. Hartl*, J. Stegmüller*, S. Hayböck*, A. Molz*, C. Breitsamter*

* Technical University of Munich, Chair of Aerodynamics and Fluid Mechanics, Boltzmannstraße 15, 85748 Garching, Germany

Abstract

Modern, high-agility aircraft develop separation-induced leading-edge vortices and vortex flow aerodynamics in various portions of their flight envelope. At higher angles of attack, vortex-bursting results in an unsteady flow field downstream of the breakdown region. High turbulence intensities and their distinct burst frequency content can lead to structural dynamic excitation of the wing and downstream located elements such as tail planes. This aerodynamic excitation may cause dynamic aeroelastic phenomena like wing and fin buffeting. A generic wind tunnel model has been developed at the Chair of Aerodynamics and Fluid Mechanics (TUM-AER) of the Technical University of Munich (TUM) for the experimental analysis of buffeting phenomena. The full-span configuration features a $76°/40°$ double-delta wing, a pivotable horizontal tail plane (HTP) and a vertical tail. The modular design of the wind tunnel model allows investigations on flexible lifting surfaces and quasi-rigid lifting surfaces. The measurement campaign takes place at the TUM-AER low-speed wind tunnel A (WT-A). An internal six-component strain gauge balance is used to measure aerodynamic forces and moments. In addition, the model is equipped with unsteady pressure transducers and accelerometers. Furthermore, the eigenmodes of the flexible and quasi-rigid configuration are determined by a ground vibration test (GVT). Analyzing the spectral content of the pressure fluctuations it is shown that the breakdown flow exhibits a significant buffet peak. With an increasing angle of attack, a shift of the dominant frequencies of the buffet peaks to lower frequencies can be observed. Considering the aerodynamic excitation, no significant differences between the flexible configuration and the rigid reference case can be observed. However, in the analysis of the structural response, clear differences could be determined.

Keywords

Vortical flows; Aeroelasticity; Tail buffeting

NOMENCLATURE

Symbols

$a_{z,rms}$	RMS value of the tip acceleration	[m/s^2]
α	Angle of attack	[°]
b	Span	[m]
β	Angle of sideslip	[°]
C_L	Lift coefficient	[-]
C_{my}	Pitching moment coefficient	[-]
c_p	Pressure coefficient	[-]
c_p'	Fluctuations of the pressure coefficient	[-]
$c_{p,rms}$	RMS value of the pressure coefficient	[-]
c_r	Root chord	[m]
δ_{HTP}	Deflection angle	[°]
F	Force	[N]
f	Frequency	[1/s]
g	Gravitational constant	[m/s^2]
k	Reduced frequency, $fc_{r,W}/U_\infty$	[-]
μ	Dynamic viscosity	[Ns/m^2]
l_μ	Wing mean aerodynamic chord	[m]
Ma	Mach number	[-]
φ	Leading-edge sweep	[°]
$Re_{1/m}$	Reynolds number, $\rho_\infty U_\infty/\mu$	[-]
ρ	Density	[kg/m^3]
s	Half span	[m]
S_{ref}	Wing reference area	[m^2]
x, y, z	Cartesian coordinates	[m]

doi: 10.25967/610509

Subscripts

dom	Dominant
F	Fuselage
HTP	Horizontal Tail Plane
W	Wing

Abbreviations

ACC	Accelerometer
AOA	Angle of Attack
AOS	Angle of Sideslip
AWTM-F	Aeroelastic Wind Tunnel Model – Full Span Configuration
AWTM	Aeroelastic Wind Tunnel Model
BM	Bending Mode
CFD	Computational Fluid Dynamics
CSM	Computational Structural Mechanics
FIR	Finite Impulse Filter
FRF	Frequency Response Function
GVT	Ground Vibration Test
HMI	Helical Mode Instability
HTP	Horizontal Tail Plane
IBV	Inboard Vortex
LE	Leading Edge
LEV	Leading-Edge Vortex
LEX	Leading-Edge Extension
MBV	Midboard Vortex
NACA	National Advisory Committee for Aeronautics
PIV	Particle Image Velocimetry
PLA	Polylactide
PSD	Power Spectral Density
PSP	Pressure-Sensitive Paint
RMS	Root Mean Square
TM	Torsional Mode
TUM-AER	Chair of Aerodynamics and Fluid Mechanics
TUM	Technical University of Munich
WT-A	Wind Tunnel A

1. INTRODUCTION

Modern high-agility aircraft are designed to cover a wide range of flight maneuvers, from efficient transonic and supersonic performance to high maneuverability at subsonic speeds. Such aircraft configurations typically feature a low aspect-ratio delta wing planform with a moderate to high leading-edge (LE) sweep angle [1]. Delta wings are subclassified into nonslender ($50° < \varphi < 60°$) and slender ($\varphi > 60°$) wings [2]. For both types, the flow separates at the LE at low angles of attack (AOA), and the shear layer rolls up, forming a leading-edge vortex (LEV) [1]. The vortex structure transfers energy to the flowfield of the upper wing surface. In particular, the flow on the wing surface is accelerated in longitudinal and wing span directions by the rotational energy of the vortex system. This results in an additional static pressure decrease on the upper wing surface. The pressure decrease goes along with an increase in maximum achievable lift [1]. The trend shows that modern high-performance aircraft configurations provide hybrid-delta wings, which take over specific functions such as aerodynamic stabilization and high maneuverability in sub-, trans-, and supersonic flight [3]. For hybrid-delta wings with multiple swept leading edges, multiple leading-edge vortices develop.

With increasing angle of attack, the vortex structures extend in size and become unstable, leading finally to vortex breakdown. The transition from stable vortical structures to vortex bursting generates extremely high turbulence intensities at the breakdown position and increased turbulence levels further downstream [1, 4]. The wake of bursting vortices contains quasi-periodic pressure oscillations which interact with the aircraft structure [1]. The coupling of aerodynamic excitation (buffet) and structural dynamic response comprising the interaction of unsteady aerodynamic forces, inertia forces and elastic forces - with the unsteady aerodynamic forces related to local flow separation and lifting surface motion (vibrations) - is referred to as buffeting [5]. The structural response of the wing and tail planes affects the maneuverability of the aircraft, reduces the lifespan of structural components and should therefore be avoided. The analysis of buffeting phenomena has been the subject of extensive research for a long time. It is of great importance for the structural dynamic design of new aircraft in both the civil and military sectors. Since the 1930s, buffeting phenomena triggered by a Junkers F 13 aircraft crash have been the subject of international scientific investigations [6]. Davis Jr. and Huston [7] formulated fundamental requirements and techniques for investigating buffeting on flexible wind tunnel models. The authors compared damping characteristics, occurring vibrational modes, and reduced resonant frequencies of different wind tunnel models with those of full-scale aircraft. They also suggested different methods of mounting models in the wind tunnel and how to avoid measurement errors.

At the Chair of Aerodynamics and Fluid Mechanics (TUM-AER) of the Technical University of Munich (TUM) numerous experimental and numerical investigations in the research field of leading-edge vortex systems and wing and tail buffeting have been conducted. Experimental investigations by Breitsamter et al. [1, 8–10] on a delta-canard configuration (EF-2000 model) focus on the phenomenon of fin buffeting. The resulting database of transient velocity and pressure measurements set a milestone in leading-edge vortex resolution of the turbulent flow field and enabled a detailed, phenomenological investigation. The analysis of the power spectral density (PSD) and the statistics of the spatial and time dependent resolution yield to existing periodicities, which can cause structural excitement at the vertical tail. Underlying the statistical analysis, Breitsamter defined the reduced frequency parameter k to predict the dominant frequencies depending on the wing geometry and the flight condition [1]. In cooperation between Airbus Defense and Space and the Chair of Aerodynamics and Fluid Mechanics, an aeroelastic wind tunnel model (AWTM) in the design of a half-span model configuration was developed and presented in Katzenmeier et al. [11]. An in-house rapid prototyping process in combination with polylactide filament (PLA) was used to manufacture dynamically scaled lifting surfaces of the AWTM. The wing and the horizontal tail plane (HTP) made of aluminum serve as a more or less rigid reference case. Katzenmeier et al. [12, 13] and Stegmüller et al. [14] perform numerical and experimental studies to investigate the vortex-structure interaction on the wing and the HTP.

The present paper is further organized as follows. Section 2 gives an overview of the developed aeroelastic wind tunnel model in full-span configuration (AWTM-F) with its modular concept, the geometry parameters and the sensor integration. Section 3 describes the flow physics of the double-delta wing and the unsteady flow phenomena. Section 4 presents the measurement methods and the measurement conditions of the experimental investigations. In section 5, the experimental results are discussed. The lift polar and the pitching moment coefficient of different rigid configurations are analyzed. Subsequently, the surface pressures for the flexible configuration (PLA) and the quasi-rigid reference configuration (aluminum) are evaluated regarding their root-mean-square values (RMS) and their frequency spectra (PSD) at different angles of attack. The rms values, as well as the acceleration spectra of the tip accelerations of the lifting surfaces, are presented. Furthermore, the results of an experimental modal analysis of the AWTM-F, determined in a ground vibration test, are discussed. Section 6 summarizes the experimental results and gives an outlook.

2. AEROELASTIC WIND TUNNEL MODEL

Based on the existing AWTM half-span wind tunnel model, an aeroelastic full-span model (AWTM-F) was developed by Stegmüller et al. [15] for experimental analysis of buffeting phenomena. The design concept is based on the idea that, on the one hand, a detailed flow-physical analysis of the occurring leading-edge vortex systems and thus of the aerodynamic excitation can be carried out on a quasi-rigid configuration. On the other hand, the aeroelastic structural response of the wind tunnel model can be investigated on a configuration with flexible lifting surfaces. Consequently, the modularity of the wind tunnel model design is of great importance.

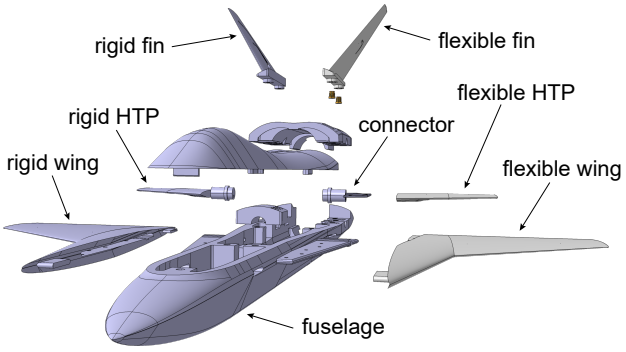

FIG 1. Modular concept of the AWTM-F wind tunnel model [15]

TAB 1. Deflection angle δ_{HTP} of the HTP with increasing angle of attack α

α	$10°$	$15°$	$20°$	$25°$	$30°$	$35°$	$40°$
δ_{HTP}	$6°$	$10°$	$13°$	$16°$	$19°$	$22°$	$25°$

2.1. Modular concept and geometry

The modular design of the wind tunnel model consists of quasi-rigid lifting surfaces of aluminum and flexible lifting surfaces of PLA, which can be attached to the rigid aluminum fuselage. The flexible components are scaled concerning a generic large-scale configuration considering structural elasticity. An overview of the applied structural dynamic scaling and the similarity rules is given in Stegmüller et al. [15]. Figure 1 illustrates the modular concept of the AWTM-F wind tunnel model. On the left-hand side, the rigid components are depicted; on the right-hand side, the flexible components are marked in lighter gray. The HTPs are rotatably mounted to the fuselage to allow different deflection angles. In contrast to the quasi-rigid HTP, which is manufactured in one piece, the flexible HTP is attached to an aluminum connector so that a strong clamping connection via the rear fuselage cover can also be provided for the flexible HTP. Table 1 shows the deflection δ_{HTP} associated with the respective angle of attack α used in the present investigation and reflecting possible trim conditions. The deflection angle δ_{HTP} is defined relative to the wing plane with pos-

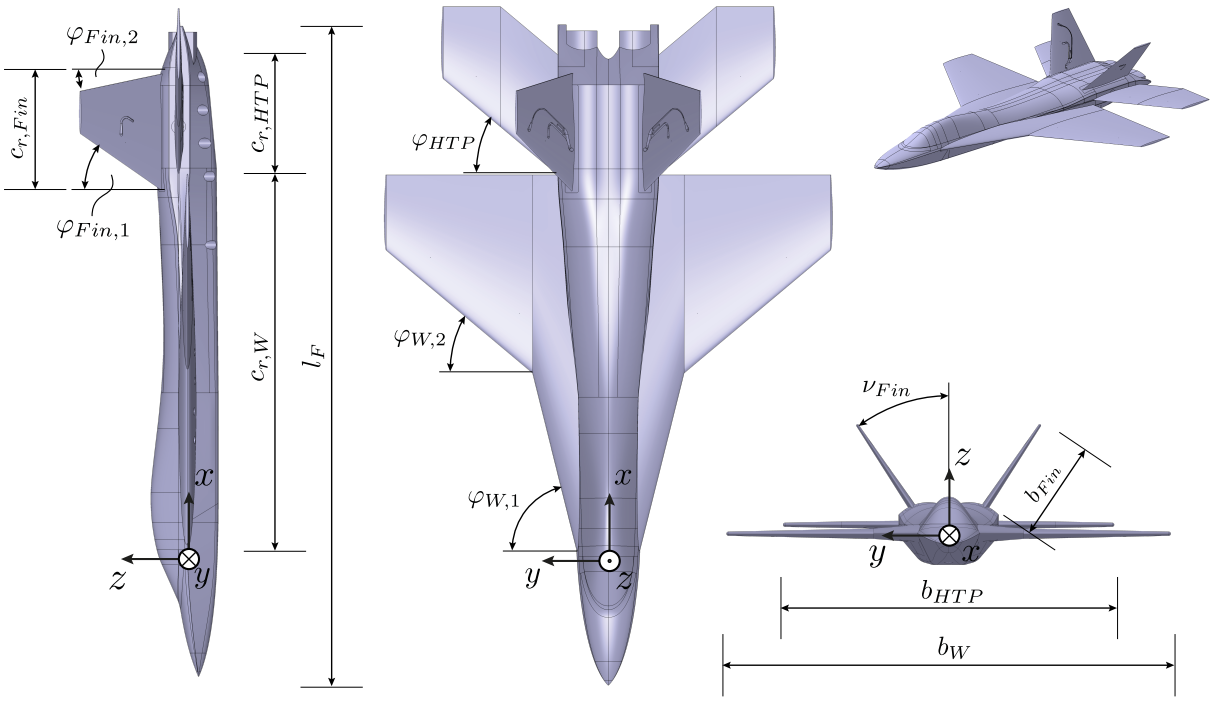

FIG 2. Geometry of the AWTM-F wind tunnel model [15]

itive values for the nose-down deflection of the HTP. Wing, HTP and vertical fin are all based on a NACA 64A-005 airfoil type.

Figure 2 gives an overview of the model geometry from different perspectives and provides the basic model parameters. The dimensions and characteristic planform parameters of the wind tunnel model are given in Table 2. Identical to the half model developed by Katzenmeier et al. [11], the AWTM-F full-span model is characterized by a double-delta wing with a sweep of $\varphi_{W,1} = 76°$ at the strake, which can be defined as leading-edge extension (LEX), and $\varphi_{W,2} = 40°$ at the outboard wind section. The fins are deflected by $\nu_{Fin} = 34°$ in relation to the x-z-plane. The leading edge of the fins features a sweep angle of $\varphi_{Fin,1} = 30°$, whereas the trailing edge has a sweep angle of $\varphi_{Fin,2} = -10°$. Given a fuselage length of $l_F = 1.1\,m$, the model has a wing root length of $c_{r,W} = 0.66\,m$ and a wingspan of $b_W = 0.74\,m$. The mean aerodynamic chord is $l_\mu = 0.427\,m$ and the wing reference area measures $S_{ref} = 0.25\,m^2$. The root length of HTP and fin is identical with $c_{r,HTP} = c_{r,Fin} = 0.2\,m$. The HTP has a span of $b_{HTP} = 0.55\,m$. In addition, the HTP's vertical position is offset by $0.015\,m$ in the positive z-direction relative to the wing plane, which provokes a higher vortex-induced turbulence intensity at the HTP [15].

2.2. Sensor integration

For the measurement of aerodynamic forces and moments as well as unsteady flow phenomena, the wind tunnel model is instrumented with an internal six-component strain gauge balance, transient pressure

TAB 2. Parameter values of the AWTM-F wind tunnel model [15]

Wing/Fuselage		HTP/Fin	
l_F	$1.1\,m$	$c_{r,HTP} = c_{r,Fin}$	$0.2\,m$
l_μ	$0.427\,m$	$c_{r,HTP}/c_{r,W}$	0.3
$c_{r,W}$	$0.66\,m$	b_{HTP}	$0.55\,m$
b_W	$0.74\,m$	b_{Fin}	$0.17\,m$
$\varphi_{W,1}$	$76°$	φ_{HTP}	$40°$
$\varphi_{W,2}$	$40°$	$\varphi_{Fin,1}/\varphi_{Fin,2}$	$30°/-10°$
S_{ref}	$0.25\,m^2$	ν_{Fin}	$34°$

transducers and accelerometers (ACC) [15]. Figure 3 shows the positions of the sensors. Transient pressure transducers (Kulite XCQ-093-5D) determine the differential pressure on the surface relative to the reference atmospheric pressure outside the test section. They are placed in positions where high-pressure fluctuations are expected. Furthermore, uniaxial accelerometers (PCB 352C22/NC) measure the wing tip accelerations to analyze the structural response due to buffeting. All sensors are located at the l/4-line of the respective lifting surface. Two Kulite transient pressure transducers and an accelerometer are installed on each wing, HTP, and fin. The positions of the Kulites are marked with filled circles, that of the ACC with a cross. Thus, in the case of the wing and the HTP, the pressure on the suction side can be measured at two positions. Kulite 1 refers to the inner position facing the fuselage, and Kulite 2 corresponds to the outer position on each side.

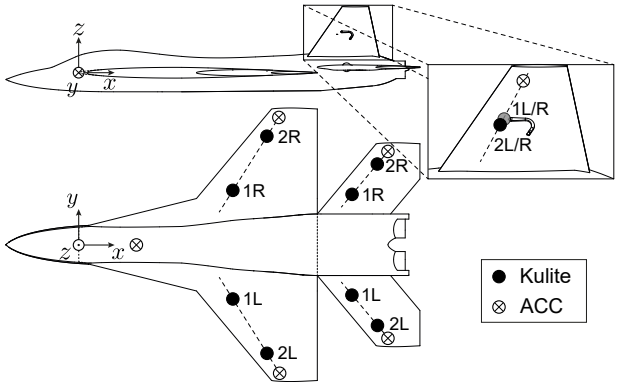

FIG 3. Sensor positions of the pressure transducers (Kulite) and accelerometers (ACC) [15]

TAB 3. Sensor positions on the AWTM-F [15]

Sensor	$\frac{x_W}{c_{r,W}}[-]$	$\frac{\lvert y_W \rvert}{s_W}[-]$	$\frac{x_{HTP}}{c_{r,W}}[-]$	$\frac{\lvert y_{HTP} \rvert}{s_{HTP}}[-]$
Kulite 1	0.651	0.400	1.144	0.500
Kulite 2	0.792	0.800	1.249	0.800
ACC	0.845	0.950	1.301	0.950
	$\frac{x_{Fin}}{c_{r,W}}[-]$	$\frac{h_{Fin}}{b_{Fin}}[-]$	$\frac{x_F}{c_{r,W}}[-]$	$z_F[mm]$
Kulite 1	1.081	0.475	–	–
Kulite 2	1.086	0.525	–	–
ACC	1.115	0.800	0.154	−34

Regarding the fin, the transient pressures are measured at an inward-facing position (Kulite 1) and at a location on the outer side (Kulite 2). The ACC are located on the tip of the wing, HTP, and fin. An additional ACC is placed in the symmetry plane of the fuselage to identify any dynamics transferred across the fuselage between individual lifting surfaces that do not result from the excitation of their specific eigenmodes.

The positions of the sensors are shown in Table 3. The origin of the body-fixed coordinate system concerning the x- and y-direction is located at the apex of the unblended wing planform at a distance of $190\,mm$ from the nose. In the z-direction, the origin is located in the wing plane. The x-positions are each referenced to the wing root length $c_{r,W}$. The y-positions at wing and HTP are related to their respective half span s_W and s_{HTP}. The spanwise positions of the sensors at the fin are referenced to the ratio of the value on the h-axis and the span b_{Fin}.

3. FLOW PHYSICS

In the following, an overview of the flow physics of the double-delta wing configuration at subsonic speeds is given. Furthermore, the unsteady flow phenomena leading to structural dynamics excitations of the AWTM-F wind tunnel model are described.

3.1. Vortex topology on a 76°/40° double-delta wing

At subsonic flow conditions, two primary vortices are formed at the leading edge of each wing. Even at small angles of attack, the pressure-induced flow around the highly swept leading edge can no longer follow the wing contour. The boundary layers of the pressure and suction sides roll up with the entrained flow to form a large-scale leading-edge vortex. When fully developed, the inboard strake-vortex extends up to the apex and rolls up along the leading edge of the strake. A second primary vortex (wing-vortex) is formed at the kink of the leading edge. The vortex core is characterized by strongly increased axial velocities, low static pressure, and a high dissipation rate [1]. Low static pressure in both vortex cores causes the strake vortex and the wing vortex to move toward each other and start interacting [16]. Figure 4 gives a simplified illustration of the vortex topology and vortex bursting points on a $76°/40°$ double-delta wing at $\alpha = 20°$ [16]. Vortex bursting is characterized by an abrupt divergence of vortex streamlines and a sudden increase in the vortex diameter [17]. The flow field downstream of the bursting point is dominated by large-scale turbulent structures, which decay into smaller vortices and finally dissipate. With increasing angle of attack, the bursting locations move further upstream, so increasingly larger portions of the wings are affected by turbulence and produce less lift. On a $76°/40°$ double-delta wing, the wing-vortex is generally weaker and less stable than the strake-vortex due to the lower sweep of the outer wing section [16].

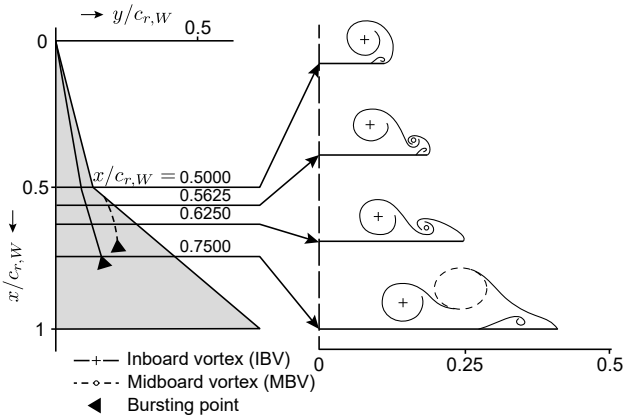

FIG 4. Vortex interaction on a $76°/40°$ double-delta wing at $\alpha = 20°$, adapted from Verhaagen et al. [16]

3.2. Unsteady flow phenomena - cause of buffeting

Unsteady flow phenomena have a significant influence on the stability and control of an aircraft configuration in vortex-dominated flows, especially on delta wing configurations. The flow field downstream of the breakdown position of the LEV consists of high turbulence intensities associated with substantial velocity and pressure oscillations [1]. These quasi-periodic

oscillations arise from a helical mode instability (HMI) of the breakdown flow [4]. The breakdown position of the leading-edge vortex system shifts further upstream as the AOA increases. The spectra of velocity fluctuations within the HMI exhibit a narrow-band region where the dominant frequency f_{dom} occurs. The turbulent kinetic energy is thus concentrated in a narrow frequency band. A determination of the dominant reduced frequency k_{dom} as a function of wing geometry (leading-edge sweep φ_W) and flight condition (flight speed U_∞, angle of attack α) was introduced by C. Breitsamter [1]. The wake instability excites the wing and the tail structure to vibrate in its natural frequencies, predominant in the 1st bending and the 1st torsional modes, leading to buffeting phenomena. The fluid-structure interaction also leads to a coupling or influence between the vibrations of the elastic structure at the fin and the oscillations of the vortex breakdown position. The chain of events of the fluid-structure interaction leading to fin buffeting is shown in Fig. 5.

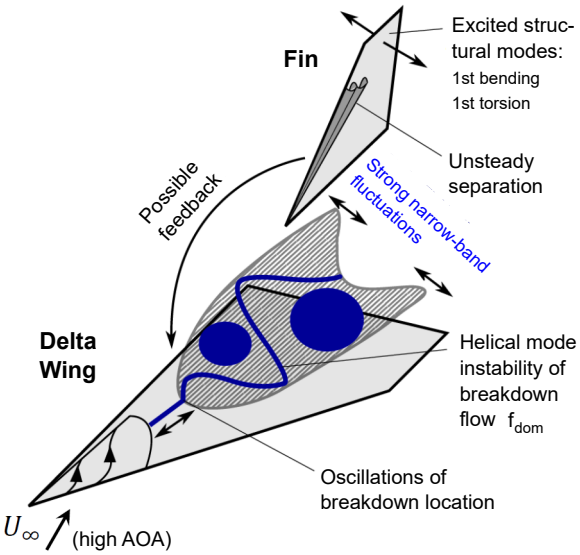

FIG 5. Fluid–structure interaction of leading-edge vortex bursting and elastic fin, adapted from Breitsamter [1]

4. EXPERIMENTAL INVESTIGATION

4.1. Measurement methods

Wind tunnel measurements are performed with the quasi-rigid reference case and with the fully flexible version of the AWTM-F. The model is mounted on a two-axis support using a rear sting, which is mounted on a turn table. This allows the adjustment of the angle of attack and the angle of sideslip of the wind tunnel model. In order to introduce as few additional dynamic effects as possible into the system, the sting has no roll angle adjustment. Force and moment measurements with the internal six-component strain gauge balance are performed separately from those with transient pressure transducers and accelerometers. In the present investigations, only the transient pressures and accelerations of the left-hand side of the AWTM-F are considered.

4.2. Ground Vibration Test

A ground vibration test was performed on the AWTM-F wind tunnel model to investigate the structural dynamics and to determine the eigenmodes and associated eigenfrequencies. The modal analysis was conducted on both the quasi-rigid configuration (aluminum) and the flexible configuration (PLA). The experimental setup of the GVT is shown in Fig. 6. The GVT was performed with the wind tunnel model installed at the support in the test section to ensure the same conditions as in the wind tunnel test. The main components for the experimental modal analysis are the mechanical structural excitation, the accelerometers for structural analysis and the data acquisition system for recording and further processing the measurement data. Two modal exciters (electrodynamic shakers) were used to excite the structure. The respective components were excited in several measurement runs to determine the eigenmodes on the wing, HTP and fin. The sinusoidal excitation was conducted in the frequency range from $f_s = 5\,Hz$ to $f_s = 400\,Hz$ at an force amplitude of $F = 0.25\,N$ to $F = 2.0\,N$. The structural dynamic response was determined using uniaxial accelerometers. Based on the excitation and the structural response, both the frequency response function (FRF) and the eigenmodes of the lifting surfaces could be extracted.

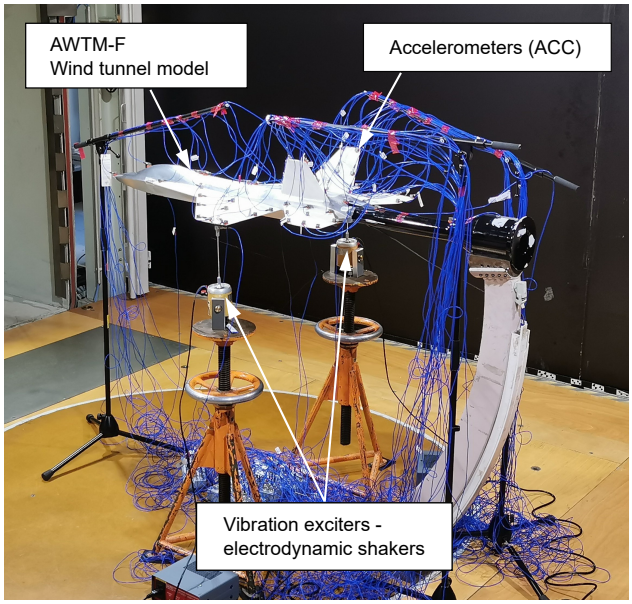

FIG 6. Experimental setup of the ground vibration test (GVT), investigation of the flexible configuration (PLA)

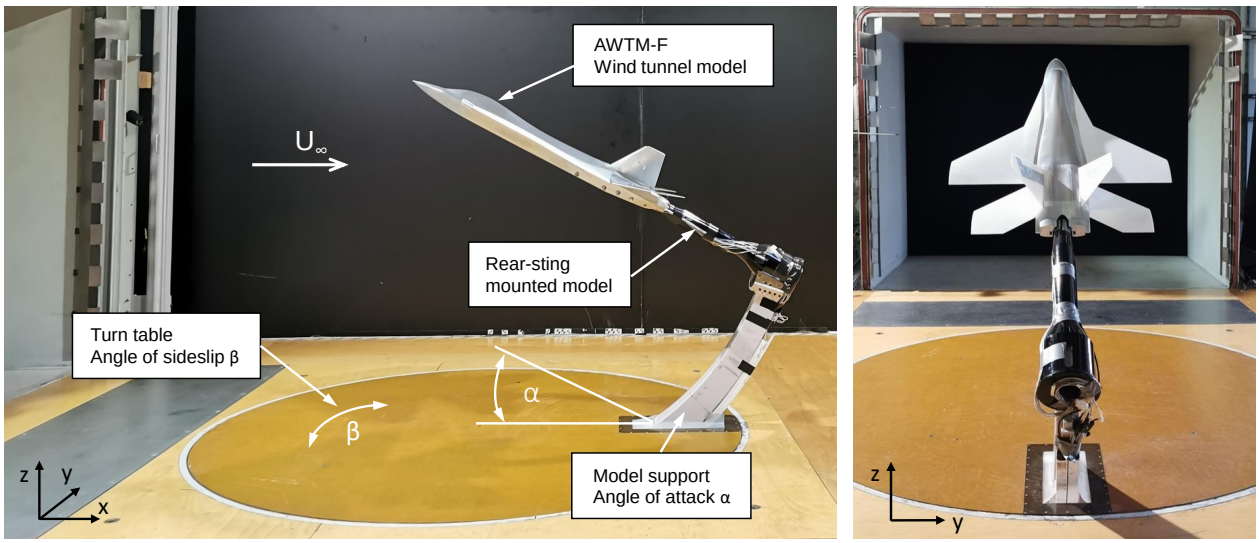

FIG 7. Installation of the AWTM-F wind tunnel model in the test section of WT-A for $\alpha = 30°$ and $\beta = 0°$

TAB 4. Wind tunnel measurement conditions

Parameter	Value
Mach number Ma	$0.15\,[-]$
Reynolds number $Re_{1/m} = \frac{\rho_\infty U_\infty}{\mu}$	$3.2 \cdot 10^6\,1/m$
Freestream velocity U_∞	$51\,m/s$
Angle of attack α	$0° - 40°$

4.3. Measurement conditions

The measurement campaign takes place at the low-speed wind tunnel A of the Chair of Aerodynamics and Fluid Mechanics of the Technical University of Munich. Figure 7 shows the wind tunnel model installed in the test section of the WT-A. The Göttingen type wind tunnel has an open test section of 1.80 m in height and 2.40 in width, with a test section length of 4.80 m. With an open test section, the maximum speed is $65\,m/s$ with a turbulence intensity in each coordinate direction of less than $0.4\,\%$. Table 4 summarizes the measurement conditions of the wind tunnel investigations. The Reynolds number related to the freestream velocity is $Re_{1/m} = 3.20 \cdot 10^6\,1/m$, which corresponds to a required freestream velocity of about $U_\infty = 51\,m/s$ and a Mach number of about $Ma_\infty = 0.15$. Thus, at all angles of attack, fully turbulent boundary layers are present to form the large-scale leading-edge vortex system. Experimental investigations are performed in an angle of attack range between $\alpha = 0°$ and $\alpha = 40°$ with a measurement time of $10\,s$. The sampling frequency of the force and moment measurements with the internal six-component balance was $f_s = 800\,Hz$. For the transient pressure and acceleration measurements, a sampling frequency of $f_s = 5120\,Hz$ was used. The setup and accuracy of the measurement methods described are published in Stegmüller et al. [15].

5. RESULTS AND DISCUSSION

In this section, the results from the experimental investigations on the AWTM-F wind tunnel model are analyzed and discussed. The focus of these investigations is on fluid-structure interaction and aeroelastic vibration effects in a vortex-dominated flow. For this purpose, a detailed flow-physical analysis of the occurring unsteady flow phenomena is conducted in the first part. In the second part, the dynamic structural response and buffeting phenomena are determined on the aeroelastic wind tunnel model for both the flexible and rigid reference configurations.

5.1. Forces and Moments

An additional non-linear lift component above a certain angle of attack characterizes the lift polar of high-agility aircraft configurations. The fully developed leading-edge vortex system leads to an increase of the axial velocity component on the suction side and thus generates a high suction level on the upper wing surface. As the angle of attack increases, the structure of the vortex core changes and the phenomenon of vortex bursting occurs. This is characterized by a divergence of the vortex streamlines around a region of stagnant flow, causing the vortex cross-section to expand abruptly. Therefore, the bursting of the primary vortex system leads to a reduction of the suction peak and subsequently to a significant decrease of the total lift [1]. Figure 8a compares the lift polars of four rigid AWTM-F wind tunnel model configurations. The AWTM-F equipped with (i) wing, HTP (deflection $\delta_{HTP} = 0°$) and fin, (ii) with wing and HTP ($\delta_{HTP} = 0°$) and (iii) with wing and fin is presented as well as (iv) the configuration with the wing only. For all AWTM-F configurations, the vortex-induced nonlinear lift can be observed from $\alpha = 8°$. The vortex breakdown over the wing leads to a sudden drop of the lift gradient at $\alpha = 16°$. The drop of the lift gradient is more pronounced in

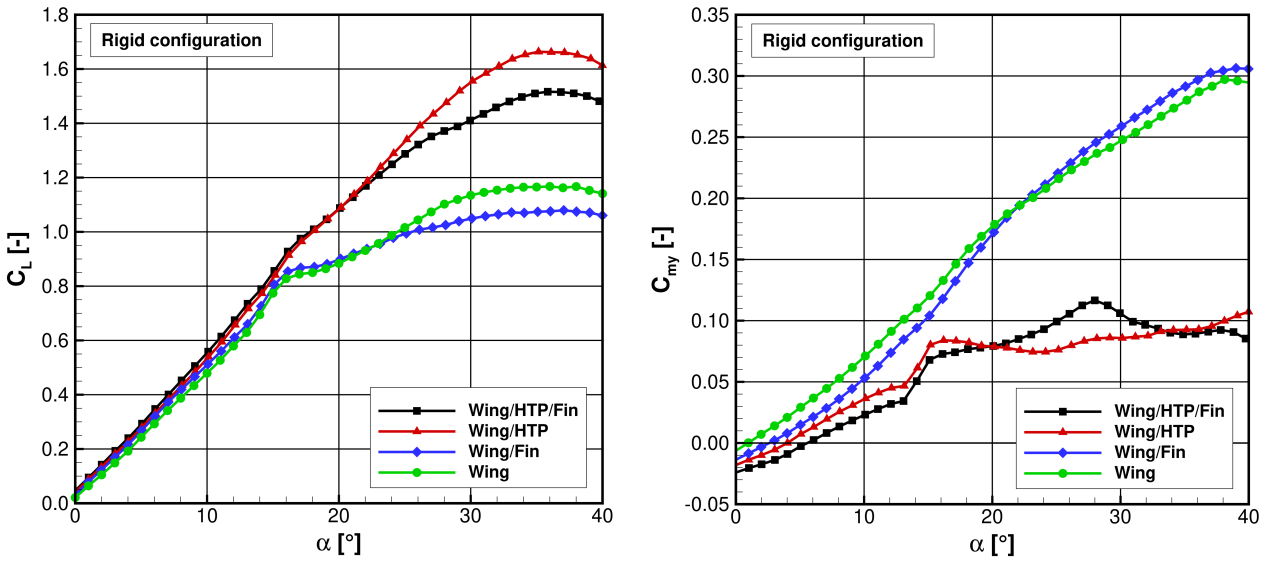

(a) Lift coefficient C_L **(b) Pitching moment coefficient C_{my}**

FIG 8. C_L and C_{my} of several $76°/40°$ AWTM-F configurations (rigid), $\alpha = 0°$ - $\alpha = 40°$, $\beta = 0°$, $U_\infty = 51\,m/s$, $Re_{1/m} = 3.20 \cdot 10^6\,1/m$

the configurations with HTP than in comparison to the configurations without HTP. It can be observed that the fin causes a significantly smaller increase in the lift coefficient from about $\alpha = 22°$ compared to the respective configuration with HTP or without HTP. The fins contribute to a negative lift increment from about $\alpha = 22°$, which results in a lower $C_{L,max}$. The maximum lift coefficient is reached from $\alpha = 36°$ to $\alpha = 38°$ for all configurations. The transition from near-stall conditions to the post-stall flight domain occurs in this angle-of-attack range. Above an angle of attack of $\alpha = 38°$ the flight domain is in the post-stall region, characterized by a negative lift gradient.

In Fig. 8b, the polars of the pitching moment coefficient of the four AWTM-F configurations are shown. A positive pitching moment coefficient ($C_{my} > 0$) means a nose-up moment and a negative pitching moment coefficient ($C_{my} < 0$) means a nose-down moment. For the configurations with HTP, a steep increase in the pitching moment polar can be seen between $\alpha = 13°$ and $\alpha = 15°$. This occurs significantly earlier than the change in the lift polar from $\alpha = 16°$ in Fig. 8a. The vortex breakdown position has already reached the HTP at $\alpha = 13°$, which has a much stronger influence on the pitching moment coefficient than on the lift coefficient due to the larger lever arm. For the configurations without HTP, a stronger increase in the pitching moment coefficient is observed from an angle of attack of $\alpha = 15°$, which corresponds better to the strong kink of the lift gradient at $\alpha = 16°$ (Fig. 8a). Furthermore, it can be seen in Fig. 8b that for the two configurations with HTP, the presence of the fin in the angle-of-attack range between $\alpha = 20°$ and $\alpha = 33°$ generates an additional positive pitching moment compared to the configuration without the fin.

5.2. Surface pressures

In the following, an overview of the evaluated surface pressures measured with transient pressure transducers (section 4.3) on the flexible and rigid AWTM-F configuration is given. For the measurements, the corresponding deflection angle of the HTP δ_{HTP} was set for each measured angle of attack. The corresponding values are given in Table 1.
Figures 9 and 10 show the rms pressure coefficient $c_{p,rms}$ of the unsteady pressure fluctuations at the sensor positions of the left wing, left HTP and left fin (Fig. 3), in the angle-of-attack range from $\alpha = 10°$ to $\alpha = 40°$. With a shift of the vortex bursting point upstream in front of the sensor position, the rms values increase. This agrees with the development of $c_{p,rms}$ for the wing in Fig. 9a, where the rms values at sensor position 1 increase at $\alpha = 22.5°$. Due to the expected post-stall region at $\alpha = 38°$, the pressure fluctuations decrease significantly. At sensor position 2L, the peak of the rms value is already reached at $\alpha = 27.5°$, but $c_{p,rms}$ rises already from $\alpha = 20°$ upwards and has a higher level than the sensor position 1L. This indicates that the outer region of the wing, which is dominated by the midboard vortex (MBV), is affected by the vortex bursting earlier. In contrast, the inner region, influenced by the inboard vortex (IBV), is subject to more significant pressure fluctuations at higher angles of attack. The peak at sensor position 2L for $\alpha = 15°$ is assumed to be caused by vortex bursting of the MBV. In the comparison between the flexible and the rigid configuration, clear differences in the rms values $c_{p,rms}$ of the wing in Fig. 9a can be observed. Particularly for the inner sensor position 1L, the pressure fluctuations are larger for the rigid configuration than for the flexible one for most angles of attack.

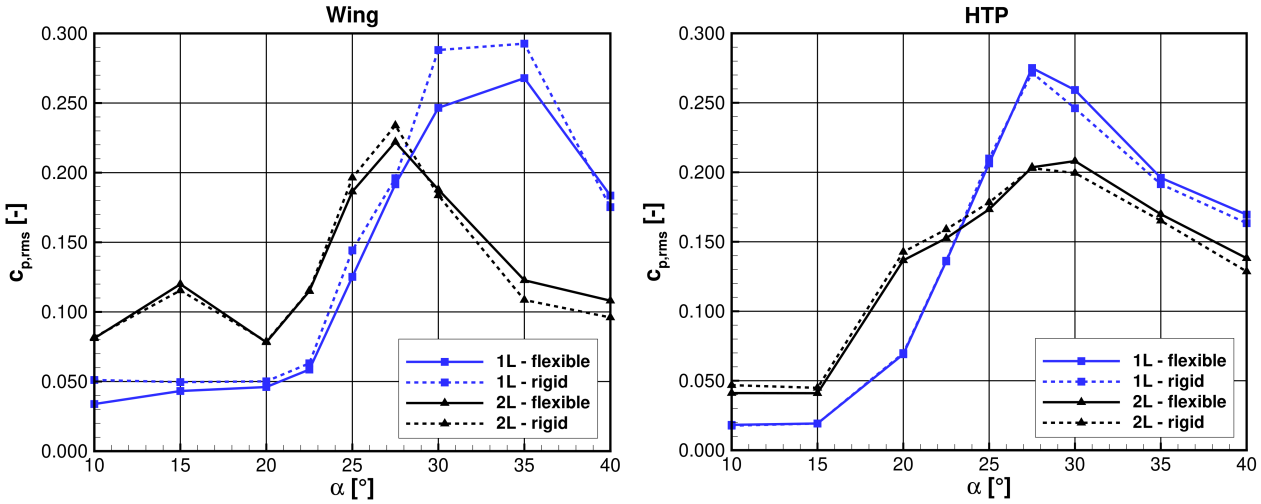

(a) $c_{p,rms}$ at the wing (b) $c_{p,rms}$ at the HTP

FIG 9. RMS value of the pressure coefficient $c_{p,rms}$ for the flexible and rigid AWTM-F configuration (wing and HTP), $\alpha = 10°$ - $\alpha = 40°$, $\beta = 0°$, $U_\infty = 51\,m/s$, $Re_{1/m} = 3.20 \cdot 10^6\,1/m$

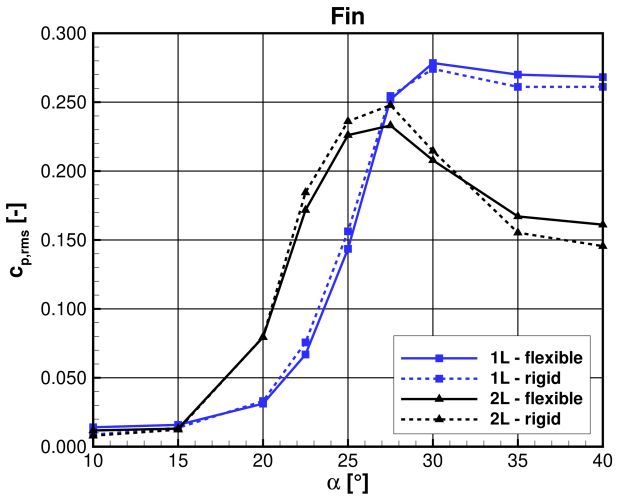

FIG 10. RMS value of the pressure coefficient $c_{p,rms}$ for the flexible and rigid AWTM-F configuration (fin), $\alpha = 10°$ - $\alpha = 40°$, $\beta = 0°$, $U_\infty = 51\,m/s$, $Re_{1/m} = 3.20 \cdot 10^6\,1/m$

Due to the downstream position of the HTP compared to the wing, it is influenced by vortex bursting even at lower angles of attack. For this reason, the pressure fluctuations in the form of the $c_{p,rms}$ values, as shown in Fig. 9b, increase already for $\alpha = 15°$ upwards. The pressure fluctuations at the HTP are very similar for the flexible and the rigid configuration at both positions in the considered angle of attack range, with slightly lower $c_{p,rms}$ values from $\alpha = 27.5°$ upward for the rigid reference case. The pressure fluctuations decrease continuously from $\alpha = 27.5°$ at the inner position (1L) and from $\alpha = 30°$ at the outer position (2L). As with the HTP, the pressure fluctuations for the fin, shown in Fig. 10, increase from $\alpha = 15°$ upward. This indicates that the breakdown position of the vortex system at $\alpha = 15°$ is already in the area of the fin. While the pressure fluctuations at the outer sensor position (2L) decrease again from $\alpha = 27.5°$ upwards, the $c_{p,rms}$ value at the inner sensor position (1L) decreases slightly above $\alpha = 30°$. In the comparison between the flexible configuration and the rigid reference configuration, the higher pressure fluctuations at $\alpha = 27.5°$ at the outer sensor position (2L) of the rigid fin are especially noticeable, while the values are almost identical for the inner position (1L) and match those of the rigid case of the outer position (2L). The flexible structure of the wing, the HTP and the fin influence to some extent the magnitude of the pressure fluctuations in terms of $c_{p,rms}$. Considering the aerodynamic excitation (buffet) related to the pressure fluctuations, slight differences can be observed between the flexible and the rigid configuration with very similar curve characteristics.

5.3. Analysis of the buffet pressure spectra

For the investigation of the aerodynamic excitation with respect to buffeting, the power spectral densities (PSD) of the pressure fluctuations c_p' on the surface of the wing, the HTP and the fin are analyzed for the flexible and rigid configuration for two different sensor positions as a function of the angle of attack. For the evaluation of the pressure spectra, a 1-D median filter of 1st order and a Savitzky-Golay finite impulse filter (FIR) of 1st order and a frame length of 51 Hz is used for denoising the initial averaged noisy signal in the frequency domain [18].

The following analysis focuses on the buffet pressure spectra of the fins since a strong aerodynamic excitation occurs, especially at the vertical tail. Figure 11 shows the power spectra of the flexible fin on the left-hand side and those of the rigid fin on the right-hand side between $\alpha = 10°$ and $\alpha = 40°$ for the sensor positions 1L (fin inboard) and 2L (fin outboard). In the higher angle of attack range from $\alpha = 20°$, the so-called buffet peak can be seen in both the flexible

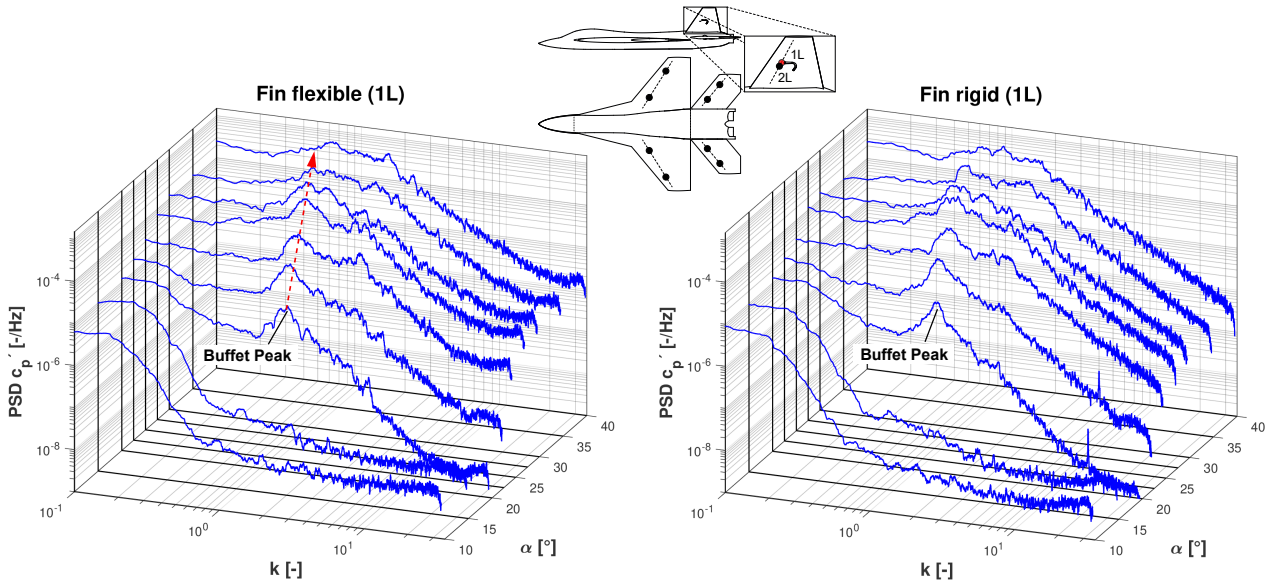

(a) PSD c_p' on the surface of the fin at sensor position 1L (inboard)

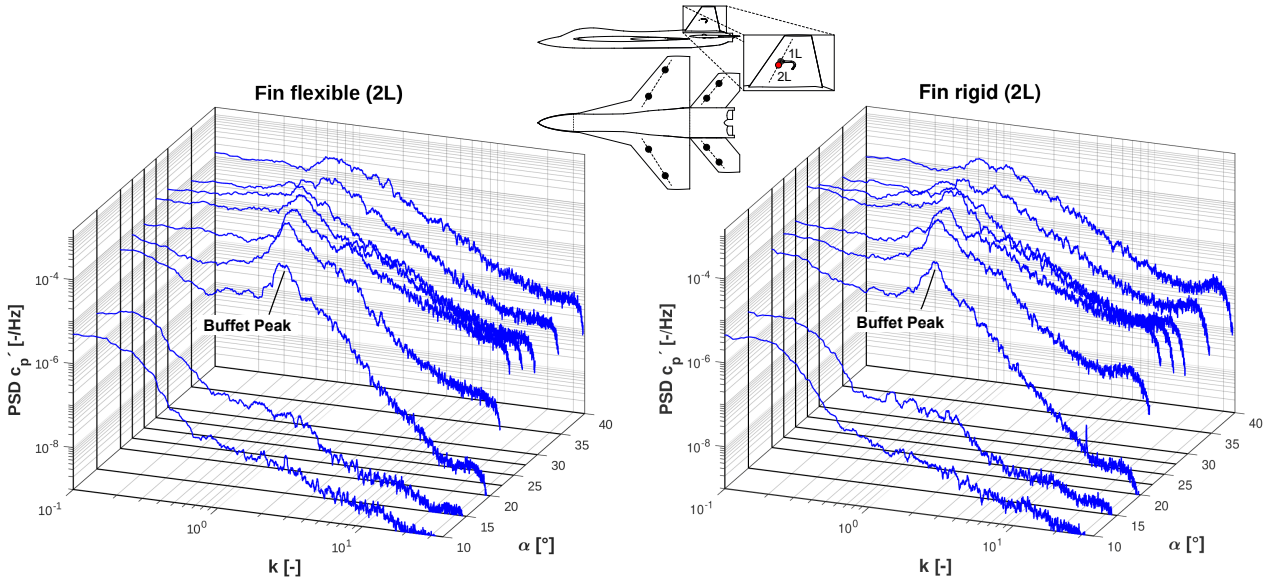

(b) PSD c_p' on the surface of the fin at sensor position 2L (outboard)

FIG 11. Power Spectral Densities (PSD) of the pressure fluctuations c_p' of the flexible and rigid fin (sensor position 1L and 2L) for different angles of attack; $\alpha = 10° - \alpha = 40°$, $\beta = 0°$, $U_\infty = 51\,m/s$, $Re_{1/m} = 3.20 \cdot 10^6\,1/m$

and rigid configuration for both sensor positions (1L and 2L). The buffet peaks in the pressure spectra confirm the theory described in section 3.2 that the vortex breakdown comes with a helical mode instability and the pressure fluctuations are dominated by quasi-periodic oscillations [1, 4, 19]. These peaks are characterized by a narrow-band concentration of turbulent kinetic energy, which can be assigned to a dominant frequency k_{dom}. The buffet peaks are shifted toward lower reduced frequencies ($k = f \cdot c_{r,W}/U_\infty$) with increasing angle of attack. In the pressure spectra for the flexible configuration (1L) in Fig. 11a, for example, a shift of the dominant frequencies from $k_{dom} = 1.40$ at $\alpha = 20°$ to $k_{dom} = 0.89$ at $\alpha = 30°$ can be observed. Breitsamter [1] explains the buffet peak shift by an expanding cross-section of the burst vortex core with increasing distance to the vortex breakdown location and thus with increasing angle of attack and the associated forward movement of the vortex breakdown position. The wavelength of the helical mode instability (HMI) increases downstream due to the expansion of the vortex cross section and the corresponding dominant frequency decreases. In the higher angle-of-attack range from $\alpha = 30°$, the pressure spectra become more broadband for all configurations, shown in Fig. 11, and no clear buffet peak can be identified. The broadband spectrum is due to the fact that in the higher angle-of-attack range, the broadband vortex core flow also exerts a more substantial influence in the burst vortex wake [19]. In Fig. 11a, the

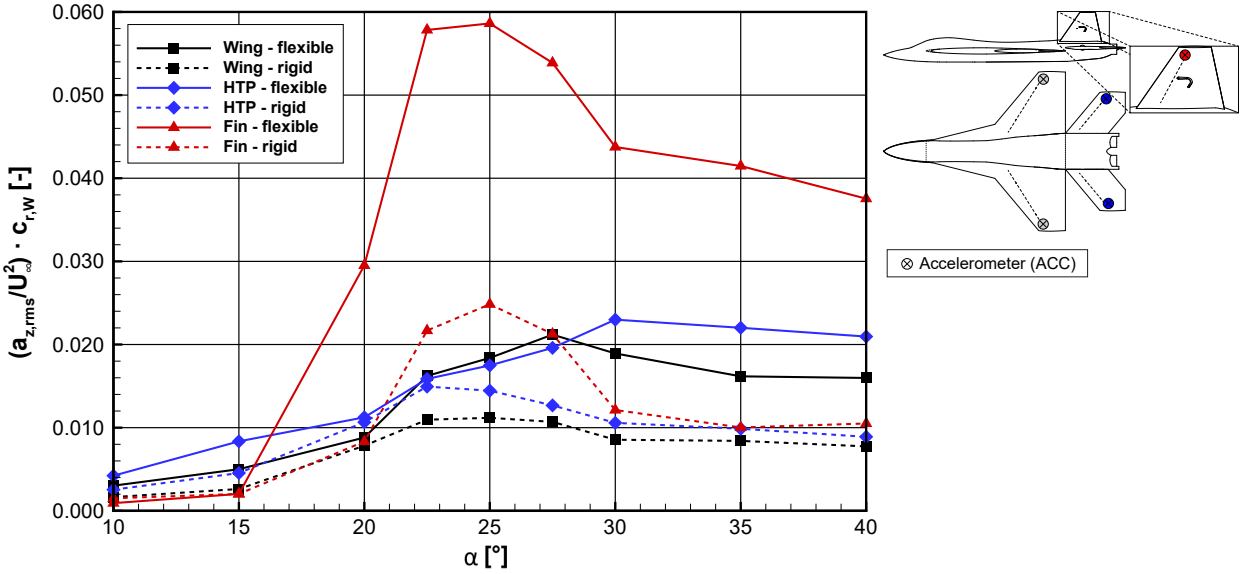

FIG 12. RMS value of the vertical tip accelerations $a_{z,rms}$ of wing, HTP and fin for the flexible and rigid configuration; $\alpha = 10°$ - $\alpha = 40°$, $\beta = 0°$, $U_\infty = 51\,m/s$, $Re_{1/m} = 3.20 \cdot 10^6\,1/m$

peaks in the power spectral densities for the sensor position 1L can be identified from $\alpha = 20°$ upward for the flexible and the rigid fin. This is consistent with the observations regarding the $c_{p,rms}$ values in Fig. 10 for sensor position 1L (fin inboard), which increase significantly from $\alpha = 20°$ due to vortex bursting. No quantitative differences can be observed in the pressure spectra between the flexible configuration and the quasi-rigid reference configuration with regard to the dominant frequencies and the characteristics of the buffet peaks. Starting from a dominant frequency of $k_{dom} = 1.40$ for the flexible configuration and $k_{dom} = 1.38$ for the rigid configuration for $\alpha = 20°$, a shift to lower dominant frequencies with increasing angle of attack can be observed in both cases. In Fig. 11b, as in the case of the sensor position 1L, the buffet peaks in the pressure spectra of the sensor position 2L for both the flexible and the rigid configuration can be identified especially for angles of attack higher than $\alpha = 20°$. The analyzed buffet peaks in the PSD of the pressure fluctuations act as an aerodynamic excitation input and are responsible for the structural response and the occurring buffeting phenomena.

5.4. Analysis of the vertical tip accelerations

In this section, the dynamic structural response of the AWTM-F will be analyzed for both the flexible configuration (PLA) and the quasi-rigid reference configuration (aluminum). As part of the experimental investigations, the vertical tip accelerations of the wing, the HTP and the fin are measured with uniaxial accelerometers, see section 2.2. In Fig. 12, the rms values of the acceleration $a_{z,rms}$, normalized by the product of the inverse square freestream velocity U_∞^2 and the wing root chord $c_{r,W}$, in an angle-of-attack range from $\alpha = 10°$ to $\alpha = 40°$ are shown. The tip accelerations of the wing, HTP and fin show a qualitatively similar curve for increasing angle of attack in the rigid case with qualitative differences between $\alpha = 20°$ and $\alpha = 30°$. In this angle-of-attack range, the largest accelerations occur at the fin, the second largest at the HTP and the smallest at the wing.

Considering the flexible configuration, significant differences occur between the individual lifting surfaces. As expected, the flexible components react more sensitively to aerodynamic excitation. For the flexible wing and HTP, the measured tip accelerations at $\alpha = 15°$ are slightly higher compared to the rigid reference case. In contrast, a similar curve between rigid and flexible configurations can be observed for the fin for an increasing angle of attack up to $\alpha = 15°$. In the angle-of-attack range from $\alpha = 15°$ to $\alpha = 22.5°$ the rms values of the tip acceleration at the flexible fin increases strongly. The abrupt increase in acceleration at $\alpha = 15°$ is a substantial indication that buffeting already occurs on the fin at this angle-of-attack range. This result is consistent with the evaluation of the lift coefficient C_L in section 5.1, where a reduction in the lift gradient can be observed from $\alpha = 16°$ due to vortex breakdown. The flowfield of the burst vortex creates a strong impact on the fins as the annular region of local turbulence maxima associated with the burst vortex system fully envelops the surfaces [1]. From a maximum value of $a_{z,rms,n} = 0.058$ at $\alpha = 25°$, a decrease in the rms values of the vertical tip acceleration occurs at the fin. Between $\alpha = 25°$ and $\alpha = 27.5°$ a moderate decrease and between $\alpha = 27.5°$ and $\alpha = 30°$ a stronger decrease can be observed. At $\alpha = 30°$ the gradient of the curve changes and a continuous decrease is observed up to a value of $a_{z,rms,n} = 0.037$ in the post-stall region at $\alpha = 40°$. Compared to the fin, the rms values of the vertical tip accelerations

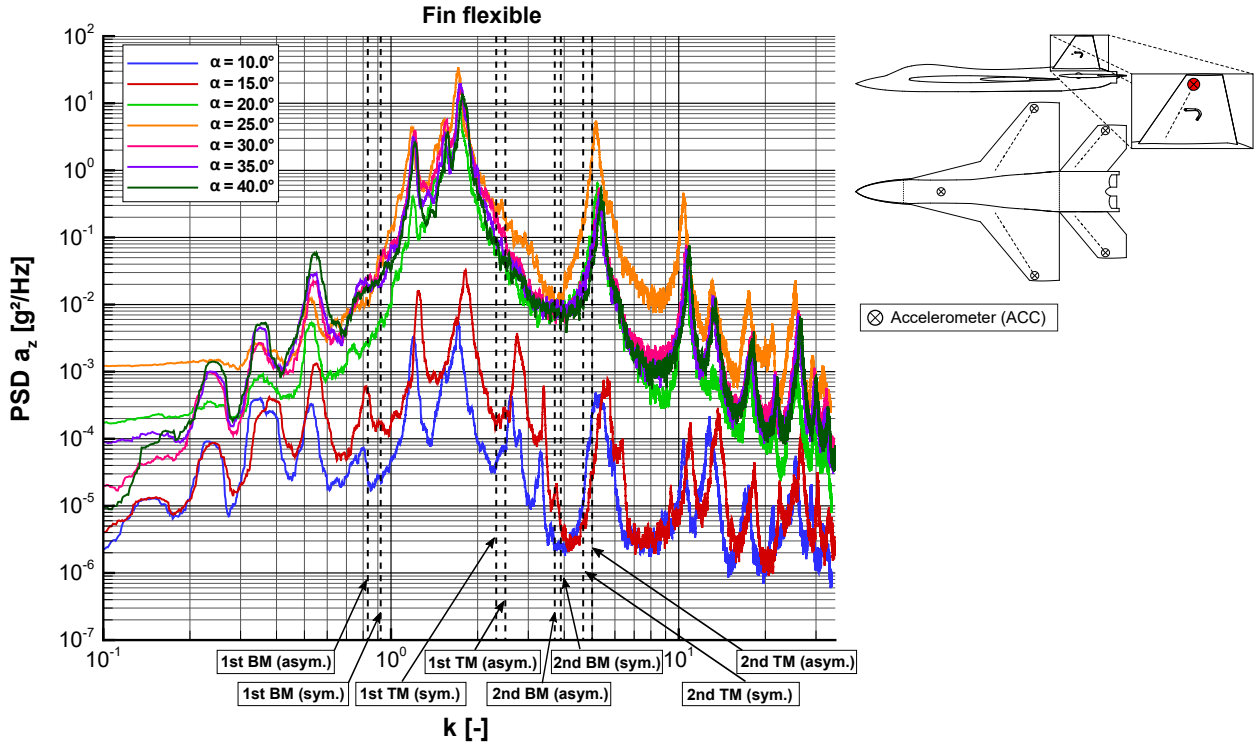

FIG 13. Power Spectral Densities (PSD) of the tip acceleration a_z of the flexible fin for different angles of attack; $\alpha = 10°$ - $\alpha = 40°$, $\beta = 0°$, $U_\infty = 51\,m/s$, $Re_{1/m} = 3.20 \cdot 10^6\,1/m$

on the wing and HTP increase from $\alpha = 20°$. At $\alpha = 22.5°$, significantly lower values are observed on the wing and HTP compared to the fin. From an angle of attack of $\alpha = 27.5°$, a decrease in the vertical tip acceleration of the flexible wing can be observed.
It can be summarized that in contrast to the aerodynamic excitation, described in section 5.3, clear differences between the flexible configuration and the rigid reference configuration can be seen in the structural response. The flexible components are strongly excited and react more sensitively to unsteady flow phenomena in the aerodynamic excitation.

5.5. Analysis of the tip acceleration spectra of the flexible fins

The pressure fluctuations at the wing, the HTP and the fin, which are analyzed in section 5.3, lead to an excitation of vibrations of the aircraft structure. The flexible configuration is significantly more sensitive to unsteady aerodynamic flow phenomena in the structural excitation investigated in section 5.4. For this reason, this section focuses on evaluating the structural dynamics response at the flexible configuration, specifically at the fin. The structural response to the aerodynamic excitation input (buffet) is investigated by evaluating the power spectral densities of the measured accelerations of the fin tip. The structural dynamics response can only occur at specific structural frequencies called eigenmodes. In terms of structural response, the first bending mode (1st BM) and the first torsional mode (1st TM) of the fin are relevant [5].

TAB 5. Results of the ground vibration test at the flexible fin in terms of eigenmodes, eigenfrequencies and damping (damping ratio in %)

Eigenmode	Eigenfrequency		Damping [%]
	k [-]	f [Hz]	
1st BM (asym.)	0.83	64.30	2.79
1st BM (sym.)	0.92	71.17	3.45
1st TM (sym.)	2.38	183.90	2.85
1st TM (asym.)	2.43	187.71	4.12
2nd BM (asym.)	3.73	288.56	2.04
2nd BM (sym.)	3.98	307.08	1.69
2nd TM (sym.)	4.59	346.51	3.04
2nd TM (asym.)	4.96	354.56	3.77

In contrast to the AWTM [11], the AWTM-F full-span model can also be used to investigate asymmetric eigenmodes. Figure 13 shows the PSDs of the fin tip accelerations a_z for the flexible configuration for $\alpha = 10°$ to $\alpha = 40°$. In contrast to the pressure spectra, simple averaging is used for denoising the initial averaged noisy signal of the fin tip accelerations in the frequency domain. For the purpose of assigning and evaluating the occurring frequency peaks, the determined BMs and TMs at the fin are drawn as dashed vertical lines. In order to evaluate the eigenmodes of the flexible fin, the amplitudes of the frequency response function of the ACC sensor position, described in section 4.2, are investigated. The eigenmodes of the flexible fin with the corresponding eigenfrequencies and the damping ratio in % (Lehr's

damping factor) are given in Table 5. In the angle-of-attack range between $\alpha = 15°$ and $\alpha = 20°$, a significant increase in the tip acceleration spectra can be observed over the entire frequency range. This observation is consistent with the analysis of the rms values on the flexible fin in Fig. 12. From an angle of attack of $\alpha = 15°$ a strong increase of the rms values of the acceleration $a_{z,rms}$ can be observed.

In Fig. 13 in the lower frequency range, two specific peaks occur at a reduced frequency of $k = 0.21$ ($f = 16$ Hz) and $k = 0.31$ ($f = 24$ Hz). These peaks, which cannot be assigned to any specific eigenmodes of the fin according to Table 5, also appear in the tip acceleration spectra of the wing and the fuselage. The first frequency peak is characterized by an oscillation of the AWTM-F about the lateral axis and the second peak by a torsional oscillation about the longitudinal axis. The clamp connection between the rigid rear-sting and the rigid fuselage is suspected to influence these low-frequency oscillation modes. In Fig. 13, the peak in the acceleration spectra at $k = 0.55$ ($f = 42.50$ Hz) can be assigned to the first bending mode of the wing. Due to the fact that the lifting surfaces are mounted to the fuselage by a frictional connection without damping, vibrations can be transmitted between the individual components. The peaks in the acceleration spectra at $k = 0.83$ ($f = 64.30$ Hz) and $k = 0.92$ ($f = 71.17$ Hz) can be associated with the first bending modes (1st BM) of the flexible fin, in the form of the symmetrical and asymmetrical eigenmode. In the frequency range from $k = 1.50$ to $k = 1.80$, a frequency peak with a secondary peak can be observed, which dominates the entire acceleration spectra in terms of magnitude. In this frequency range, the 1st sym. torsional mode ($k = 1.60$) and the 1st asym. torsional mode ($k = 1.65$) occur at the HTP, as well as the 1st sym. torsional mode ($k = 1.76$) and the 1st asym. torsional mode ($k = 1.80$) at the wing. Due to the high magnitude of this peak, it is assumed that the torsional modes influence each other and mode coupling occurs [20]. In comparison, the 1st sym. torsional mode of the fin occurs at $k = 2.38$ ($f = 183.90$ Hz) and the 1st asym. torsional mode at $k = 2.43$ ($f = 187.71$ Hz). The frequencies of the higher eigenmodes of the flexible fin, such as the second bending mode (2nd BM) and the second torsional mode (2nd TM), are shown in Table 5.

In Fig. 14, the dominant frequency k_{dom} of the aerodynamic excitation of the flexible fin for two different sensor positions (1L and 2L) is plotted in the angle-of-attack range from $\alpha = 20°$ to $\alpha = 40°$. The structural dynamics response of the flexible configuration will be maximum when the buffet peak approximately coincides with an eigenmode of the fin [1]. Due to the shift of the dominant frequency with increasing angle of attack, according to section 5.3, the first bending modes are excited in the investigated angle-of-attack range. In the range between $\alpha = 28°$ and $\alpha = 30°$, the dominant frequency corresponds to the eigenfrequency of the first symmetric bending mode of the flexible fin. The first asymmetric bending mode is aerodynamically excited from $\alpha = 30°$ to $\alpha = 32°$ for both sensor positions. The eigenfrequency of the first torsional mode is in a much higher frequency range than the first bending mode and does not coincide with the dominant frequency of the aerodynamic excitation.

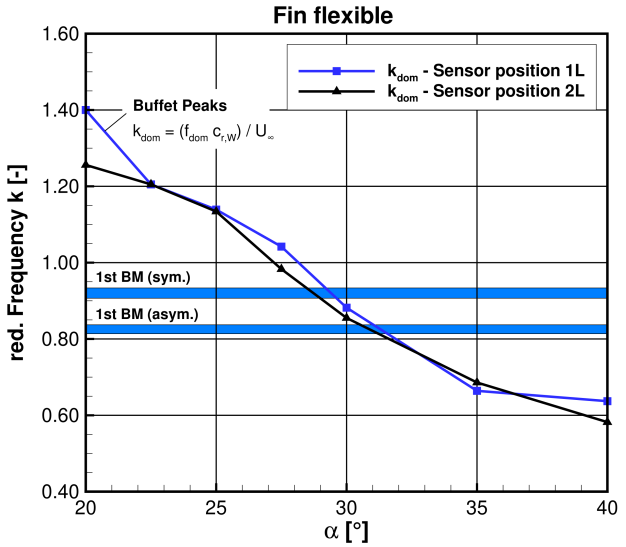

FIG 14. Dominant frequencies k_{dom} and aerodynamic excitation of the first bending mode of the flexible fin, $\alpha = 20°$ - $\alpha = 40°$, $\beta = 0°$, $U_\infty = 51\,m/s$, $Re_{1/m} = 3.20 \cdot 10^6\,1/m$

6. CONCLUSION

Experimental investigations on a modular full-span aeroelastic wind tunnel model (AWTM-F) with either rigid or flexible wings and tail planes are performed at the low-speed TUM-AER wind tunnel A to study unsteady flow phenomena and buffeting. The AWTM-F is a generic double-delta wing configuration with a pivotable horizontal tail plane and a vertical tail. The double-delta wing has a leading-edge sweep of $\varphi_{W,1} = 76°$ at the strake and $\varphi_{W,2} = 40°$ at the main wing section. Force and moment measurements are performed with an internal six-component balance to determine the lift polar and the pitching moment. In addition, the model was equipped with unsteady pressure transducers to analyze the aerodynamic excitation (buffet) and accelerometers to evaluate the dynamic structural response (buffeting). A GVT was performed to determine the eigenmodes and the corresponding eigenfrequencies.

The lift polar of the double-delta wing configuration investigated in this paper is characterized by an additional vortex-induced non-linear lift component from an angle of attack of $\alpha = 8°$. The vortex breakdown over the wing leads to a drop of the lift gradient at $\alpha = 16°$. The maximum lift coefficient is reached at about $\alpha = 36°$ for all configurations studied. The flight

state is in the post-stall region above $\alpha = 38°$, characterized by a negative lift gradient. High-pressure fluctuations downstream of the burst vortices are responsible for the potential aerodynamic excitation of the aircraft structure and the associated dynamic structural response. In the spectral analysis (PSD) of the surface pressure fluctuations, quasi-periodic oscillations occur above a certain angle of attack, which leads to an excitation of the aircraft structure. At the vertical tail (fin), distinct buffet peaks can already be identified at an angle of attack of $\alpha = 20°$ for both sensor positions (1L and 2L). As expected, a shift of the dominant frequencies of the buffet peaks to lower reduced frequencies with increasing angle of attack can be observed.

In the structural dynamics response, significant differences between the flexible and the rigid reference configuration can be observed. The flexible lifting surfaces react more sensitively to unsteady flow phenomena. The wake of the burst vortex creates a strong impact, especially on the fins, as the annular region of local turbulence maxima associated with the burst vortex system fully envelops the fin surfaces. In the ground vibration test of the AWTM-F, symmetrical and asymmetrical eigenmodes could be determined. The frequency peaks occurring in the analysis of the PSD of the fin tip accelerations correlate with the determined eigenmodes. The dominant frequencies of the aerodynamic excitation at the flexible fin coincide with the frequency of the first bending mode in the higher angle of attack range and a critical excitation of the first bending mode can be observed.

For a better understanding of the influence of the flexible components on the vortex topology and the vortex breakdown behavior, further experimental investigations have to be performed. Stereo-PIV measurements are conducted to study the upstream and downstream effects of the components on the flow field. For analyzing the unsteady pressures on the surfaces of the wing and the tail, as well as the dynamic three-dimensional structural deformation with a high spatial and temporal resolution, optical measurements with fast-response pressure-sensitive paint (PSP) and optical deformation measurements will be performed simultaneously. In terms of numerical investigations, a coupled CFD-CSM simulation is on-going to analyze the flexible configuration.

7. ACKNOWLEDGEMENTS

The funding of the presented investigations by the Deutsche Forschungsgemeinschaft (DFG Project: Charakteristiken von Strömungs-Struktur-Interaktionen bei Einwirkung von Vorderkantenwirbelsystemen, Grant-Number: BR 1511/15-1) is gratefully acknowledged. The authors would like to thank Airbus Defence and Space GmbH for performing the ground vibration test on the AWTM-F wind tunnel model.

Contact address:

patrick.hartl@tum.de

References

[1] C. Breitsamter. Unsteady flow phenomena associated with leading-edge vortices. *Progress in Aerospace Sciences*, 44(1):48–65, 2008. ISSN: 03760421. DOI: 10.1016/j.paerosci.2007.10.002.

[2] S. Hitzel. Sub- and transonic vortex breakdown flight condition simulations of the F-16XL aircraft. *Journal of Aircraft*, 54(2):428–443, 2017. ISSN: 15333868. DOI: 10.2514/1.C033246.

[3] A. Schütte and D. J. Hummel. Numerical Design Studies on the Roll Stability of a Multi-Delta-Wing Configuration. *Journal of Aircraft*, 60(3):898–914, 2023. ISSN: 15333868. DOI: 10.2514/1.C037128.

[4] I. Gursul. Review of unsteady vortex flows over slender delta wings. *Journal of Aircraft*, 42(2):299–319, 2005. ISSN: 15333868. DOI: 10.2514/1.5269.

[5] D. G. Mabey. Some aspects of aircraft dynamic loads due to flow separation. *Progress in Aerospace Sciences*, 26(2):115–151, 1989. ISSN: 03760421. DOI: 10.1016/0376-0421(89)90006-7.

[6] W. J. Duncan. Tail Buffeting. *The Journal of the Royal Aeronautical Society*, 38(278):108–137, 1934. ISSN: 0368-3931. DOI: 10.1017/s0368393100110156.

[7] D. D. Davis Jr. and W. B. Huston. The use of wind tunnels to predict flight buffet loads. *Research Memorandum NACA RM L57D25, National Advisory Committee for Aeronautics*, 1957.

[8] C. Breitsamter and B. Laschka. Fin Buffet Load Alleviation using an actively controlled Auxiliary Rudder at Sideslip. *International Council of the Aeronautical Sciences (ICAS) 2000 Congress*, 2000.

[9] C. Breitsamter. Aerodynamic active control for fin-buffet load alleviation. *Journal of Aircraft*, 42(5):1252–1263, 2005. ISSN: 15333868. DOI: 10.2514/1.8174.

[10] C. Breitsamter and A. Schmid. Airbrake-induced fin-buffet loads on fighter aircraft. *Journal of Aircraft*, 45(5):1619–1630, 2008. ISSN: 15333868. DOI: 10.2514/1.33969.

[11] L. Katzenmeier, C. Vidy, A. Kolb, and C. Breitsamter. Aeroelastic wind tunnel model for

tail buffeting analysis using rapid prototyping technologies. *CEAS Aeronautical Journal*, 12(3):633–651, 2021. ISSN: 18695590. DOI: 10.1007/s13272-021-00523-9.

[12] L. Katzenmeier, C. Vidy, L. Benassi, and C. Breitsamter. Prediction of horizontal tail buffeting loads based on URANS and DES approaches. *International Forum on Aeroelasticity and Structural Dynamics (IFASD) 2019*, 2020.

[13] L. Katzenmeier, C. Vidy, and C. Breitsamter. Using a Proper Orthogonal Decomposition representation of the aerodynamic forces for stochastic buffeting prediction. *Journal of Fluids and Structures*, 99, 2020. ISSN: 10958622. DOI: 10.1016/j.jfluidstructs.2020.103178.

[14] J. Stegmüller, L. Katzenmeier, and C. Breitsamter. Horizontal tail buffeting characteristics at wing vortex flow impact. *CEAS Aeronautical Journal*, 13(3):779–796, 2022. ISSN: 18695590. DOI: 10.1007/s13272-022-00593-3.

[15] J. Stegmüller, S. Hayböck, P. Hartl, and C. Breitsamter. Experimental Investigations of an Aeroelastic Wind Tunnel Model for Tail Buffeting Analysis. *33rd Congress of the International Council of the Aeronautical Sciences, ICAS 2022*, 4:2732–2748, 2022.

[16] N. G. Verhaagen, L. N. Jenkins, S. B. Kern, and A. E. Washburn. A study of the vortex flow over a 76/40-deg double-delta wing. *33rd Aerospace Sciences Meeting and Exhibit*, 1995. DOI: 10.2514/6.1995-650.

[17] I. Gursul. Criteria for location of vortex breakdown over delta wings. *Aeronautical Journal*, 99(985):194–196, 1995. ISSN: 00019240. DOI: 10.1017/s0001924000028372.

[18] F. M. Heckmeier, S. Hayböck, and C. Breitsamter. Spatial and temporal resolution of a fast-response aerodynamic pressure probe in grid-generated turbulence. *Experiments in Fluids*, 62(2), 2021. ISSN: 14321114. DOI: 10.1007/s00348-021-03141-7.

[19] C. Breitsamter. Turbulente Strömungsstrukturen an Flugzeugkonfigurationen mit Vorderkantenwirbeln. *Doctoral Dissertation, Technical University of Munich TUM*, 1997.

[20] T. Theodorsen. General Theory of Aerodynamic Instability and the Mechanism of Flutter. *National Advisory Committee for Aeronautics NACA, Langley Aeronautical Lab., Langley Field*, 1949.